Dalton Transactions

ROYAL SOCIETY OF CHEMISTRY

PAPER

Cite this: DOI: 10.1039/d5dt02068a

Degrees of distortion: synthesis, structure and bonding in approximately icosahedral $[Ru@Sn_{12}]^{4-}$

Sourav Mondal, †[a] Ya-Shan Huang,†[b] Zhong-Ming Sun *[b] and John E. McGrady *[a]

Received 28th August 2025,
Accepted 18th October 2025

DOI: 10.1039/d5dt02068a

rsc.li/dalton

We report here the synthesis and structural characterisation of the $[Ru@Sn_{12}]^{4-}$ anion, a new member of the icosahedral $M@E_{12}$ family of endohedral Zintl clusters. The cluster is approximately icosahedral, but a significant variance in the Ru–Sn and Sn–Sn bond lengths is a result of back-bonding from the Ru center to the Sn_{12} cage. We use density functional theory to place the structural chemistry of $[Ru@Sn_{12}]^{4-}$ into the wider context of the $M@E_{12}$ family.

Introduction

The family of endohedral Zintl clusters is an increasingly diverse one that now includes examples with many of the d-block elements,[1,2] the lanthanides and the actinides.[3–6] Applications of these clusters are beginning to emerge in materials science and catalysis,[7] but there remains an enduring fascination with the nature of the chemical bond between the endohedral metal and the cage.[8,9] These clusters are perhaps unique in their electronic flexibility, in the sense that although strong bonding interactions between the cage and the endohedral atom are certainly possible, they are not essential to the integrity of the cluster. It is possible, therefore, to find a wide spectrum of bond types within a closely-related family of clusters, and numerous reviews have been devoted to their electronic structure using density functional theory as well as wavefunction-based methods.[1,8,10–12] In this paper, we report the synthesis and crystal structure of a new member of the Zintl ion family, the 60-valence-electron ruthenium/tin cluster $[Ru@Sn_{12}]^{4-}$, in the form of its $[K(2.2.2\text{-crypt})]^{+}$ salt. The Ru center is formally in the −2 oxidation state, as it is in the 9-vertex $[Ru@Sn_9]^{6-}$ cluster reported recently by Fässler and co-workers,[13] which has proven to be an effective catalytic precursor for CO_2 reduction.[14] The $[Ru@Sn_{12}]^{4-}$ ion is approximately icosahedral but there is a significant variance in both the Ru–Sn (2.79–3.03 Å) and Sn–Sn (2.94–3.12 Å) bond lengths caused by the ionic lattice. The icosahedra in the valence isoelectronic group 9 analogues, $[Rh@Sn_{12}]^{3-}$ and $[Ir@Sn_{12}]^{3-}$ reported by Sun,[15] and Fässler,[16] respectively, are also distorted, but to a much lesser degree than found here. Moving one group further to the right, the 60-electron Pd cluster $[Pd@Pb_{12}]^{2-}$ is essentially undistorted from a perfect icosahedral geometry.[17] Group 11 analogues have not yet been crystallographically characterised, but Cui *et al.* have reported the photoelectron spectra of $[Cu@Sn_{12}]^{-}$ and $[Au@Sn_{12}]^{-}$, which are consistent with the perfectly icosahedral geometries computed by density functional theory.[18] There appears, therefore, to be a distinct correlation between the formal oxidation state of the metal (Ru^{-II}, Rh^{-I}, Pd^{0}) and the degree of distortion of the encapsulating icosahedron.

Although the undoped icosahedral Sn_{12} clusters have not been isolated in the solid state, the mono-anions, Sn_{12}^{-} and KSn_{12}^{-} have been observed by gas-phase photoelectron spectroscopy,[19] as have their Pb analogues.[20] The spectra are remarkably simple, suggesting high symmetry, and calculations indicate that the undoped Sn_{12}^{2-} species, stannasphere-ene, is perfectly icosahedral, with the 50 valence electrons occupying 13 bonding orbitals and 12 Sn $5s^2$ lone pairs, consistent with the $4n + 2$ count required for a *closo* icosahedron according to the Wade–Mingos rules.[21,22] In the $[Pd@Pb_{12}]^{2-}$ cluster, the 60 available valence electrons can be cleanly partitioned into a closed-shell d^{10} configuration at the metal with the remaining electrons making up the 50-electron closed-shell count of the icosahedron. As we move to the left in the periodic table, however, the d orbitals become more diffuse and higher in energy, increasing the driving force for back-bonding to vacant orbitals of the cage, and the distinction between metal- and cluster-based electrons becomes less clear-cut. We have shown previously that this is the origin of the distortion in $[Rh@Sn_{12}]^{3-}$, a pattern that is amplified in this new ruthenium analogue.[15] There are also two crystallographically-characterized members of the $[M@E_{12}]^{z-}$ family (M = Sn, Pb) where the total valence electron count deviates from 60. The

[a]*Department of Chemistry, University of Oxford, Inorganic Chemistry Laboratory, South Parks Road, Oxford, OX1 3QR, UK. E-mail: john.mcgrady@chem.ox.ac.uk*
[b]*State Key Laboratory of Element-Organic Chemistry, Tianjin Key Lab for Rare Earth Materials and Applications, School of Materials Science and Engineering, Nankai University, Tianjin, 300350, China. E-mail: sunlab@nankai.edu.cn*
† These authors contributed equally to this work.

first of these is 62-electron $[Au@Pb_{12}]^{3-}$,[23] where the d^{10} configuration at the metal is retained and the Pb_{12} unit is fully reduced by 2 electrons (Pb_{12}^{4-}). The icosahedron is now very strikingly distorted to an approximately D_{3d}-symmetric geometry with Au–Pb and Pb–Pb distances that vary over 0.25 Å and 0.15 Å.[12] The 58-electron cluster $[Mn@Pb_{12}]^{3-}$ is also strongly distorted (RMSD = 0.112 Å), in this case to a D_{2h}-symmetric geometry.[24] Despite the lower total valence electron count, the Pb_{12} cage is again reduced beyond the 2-level, the driving force for electron transfer to the cage in this case being the stability of the half-filled d^5 shell (Mn^{2+}). The available structural evidence suggests that is a correlation between the electron density on the E_{12} unit and the degree to which it is distorted from perfect icosahedral symmetry. In its extreme limit, electron transfer from the metal to the cage can drive the adoption of a completely different structural type, the 'fullerene-like' architecture with D_{2d} symmetry seen in $[Ru@Ge_{12}]^{3-}$ [25] that, in the absence of an endohedral metal, would be characteristic of a 60 valence-electron count at the cage.[12,26,27] In the final section of this paper, we use density functional theory to explore the trends in bonding across the 60-electron family, and to place $[Ru@Sn_{12}]^{4-}$ in the wider context of Zintl-cluster chemistry.

Experimental procedures

All operations were carried out under a nitrogen atmosphere using standard Schlenk or glovebox techniques. Ethylenediamine (Aldrich, 99%) and toluene (Aldrich, 99.8%) were freshly distilled over sodium and stored under nitrogen. 2.2.2-Crypt (4,7,13,16,21,24-hexaoxa-1,10-diazabicyclo (8.8.8) hexacosane, purchased from Sigma-Aldirich, 98%) was dried in vacuum for 12 h prior to use. The Zintl precursor phase "K_4Sn_9" was obtained by heating a stoichiometric mixture of the elements (K: >99%, Sn: 99.99% all from Aladdin) at 850 °C for 36 hours in a niobium tube. The ruthenium source, Ru (COD)Nap, was synthesized following a previously reported procedure.[28]

Synthesis of $[K(2.2.2\text{-crypt})]_4[Ru@Sn_{12}]\cdot 2en$

K_4Sn_9 (122 mg, 0.1 mmol) and 2.2.2-crypt (150 mg, 0.4 mmol) were dissolved in 3 mL ethylenediamine in a test tube inside a glovebox and stirred for 0.5 h. Ru(COD)Nap (27 mg, 0.08 mmol) was then added and the mixture was stirred for 3 h at room temperature. The resulting dark brown solution was concentrated to remove the solvent, and then redissolved in 3 mL DMF and stirred for an additional 3 h at room temperature. The resulting solution was filtered and layered with toluene to facilitate crystallization. After two weeks, black prism-like crystals of $[K(2.2.2\text{-crypt})]_4[Ru@Sn_{12}]\cdot 2en$ were obtained in a yield of 23% based on the amount of K_4Sn_9.

X-ray diffraction

Suitable single crystals were selected for X-ray diffraction analysis on a Rigaku XtalAB Pro MM007 DW diffractometer with graphite monochromated Cu Kα radiation (λ = 1.54184 Å). Using direct methods, structures were solved and refined to convergence using SHELXL-2014 and Olex2.[29–31] Non-hydrogen atoms were refined anisotropically, except for those in split positions, while all hydrogen atoms of organic groups were placed rationally using geometric considerations. Crystallographic data are available from the Cambridge Crystallographic database, CCDC 2257232.

Electrospray ionization mass spectrometry (ESI-MS)

ESI-MS analysis was conducted using an Agilent Technologies ESI-TOF-MS (6230) on an LTQ linear ion trap spectrometer. The spray voltage and capillary voltage were set to 5.48 kV and 30 V, respectively, while the capillary temperature was maintained at 300 °C.

Energy dispersive X-ray (EDX) spectroscopy

EDX analysis was conducted with a scanning electron microscope (FE-SEM, JEOL JSM-7800F, Japan), using an acceleration voltage of 20 kV and an accumulation time of 150 s for data acquisition.

DFT calculations

All DFT calculations were performed using the Amsterdam density functional (ADF) package, version 2024.101.[32] The Perdew–Becke–Ernzerhof (PBE) exchange–correlation functional[33] was used throughout, along with scalar relativistic effects in the zeroth order regular approximation (ZORA).[34] Slater-type basis sets of double polarised triple-zeta quality (TZ2P) were used,[35] and all electrons were treated as valence. The confining effect of the cation in crystalline environment was approximated using the conductor like screening model (COSMO, ε = 79.38).[36] Given the flatness of the potential energy surface (*vide infra*), we have used a very fine numerical integration grid and applied tight convergence criteria on energies and forces that are a factor of 10 smaller than the defaults. For clusters with valence electron counts other than 60, the imposition of strict I_h symmetry entails the partial occupation of degenerate orbitals (h_g for fewer than 60 electrons, g_g for more than 60). In these cases, the excess electrons or excess holes are distributed evenly over the degenerate components of the orbitals, resulting in fractional occupation numbers.

Results

Synthesis and characterisation of $[K(2.2.2\text{-crypt})]_4[Ru@Sn_{12}]\cdot 2en$, 1

$[K(2.2.2\text{-crypt})]_4[Ru@Sn_{12}]\cdot 2en$ (**1**) was synthesized according to the procedures set out in the Experimental section. The negative-ion ESI-MS of a freshly prepared solution of **1** in DMF, shown in SI, Fig. S3, confirms the presence of the parent ion in the form of the cation–dianion pair $\{[K(2.2.2\text{-crypt})][RuSn_{12}]\}^-$. More prominent features correspond to fragmentation products including the $[RuSn_{10}]^-$ ion and its cation–dianion pair, and also from the Sn_{10}^- cluster where the

endohedral metal has been lost entirely. Energy-dispersive X-ray spectroscopy (EDX, Fig. S4) also confirms the presence of Ru and Sn in a ratio consistent with the proposed formulation. Single-crystal X-ray diffraction reveals that **1** crystallizes in the triclinic space group $P\bar{1}$, with a unit cell containing one cluster anion, four $[K(2.2.2)crypt]^+$ cations and two ethylenediamine (en) molecules, with the shortest K^+–Sn contacts in excess of 6.5 Å (Fig. 2). Key bond lengths are summarized in the figure and in Table 1.

The anion adopts an approximately icosahedral architecture, very similar to those of the valence isoelectronic clusters $[Rh@Sn_{12}]^{3-}$ and $[Pt@Pb_{12}]^{2-}$. The average Ru–Sn bond length of 2.90 Å is considerably longer than those in the other known binary Ru/Sn cluster, $[Ru@Sn_9]^{6-}$ (2.641–2.700 Å), probably a consequence of the intrinsically smaller radius of the Sn_9 cage, but also longer than those in binary alloy phases (2.60–2.80 Å)[37] and in clusters where the Ru is *exo*-, rather than *endo*hedral, with respect to a Sn_x cluster, for example $[Sn_{19}\{Ru(COD)(en)\}2]^{4-}$ (2.678–2.794 Å)[37] and $[Sn_{20}\{Ru(COD)\}2]^{6-}$ (2.683–2.767 Å).[38] There are, however, some striking distortions of the icosahedron in $[Ru@Sn_{12}]^{4-}$ that lower the point symmetry from I_h to C_i. The 12 Ru–Sn bonds separate into six symmetry-distinct, mutually *trans*, pairs, the shortest of which is 2.79 Å, the longest 3.03 Å. The 20 Sn–Sn bonds are similarly separated into 10 symmetry-related pairs with bond lengths spanning 0.18 Å from the shortest (2.94 Å) to the longest (3.12 Å). As a global measure of the magnitude of distortion, we take the root mean square displacement (RMSD) of the crystallographic coordinates required to symmetrize to a perfect icosahedron: the RMSD value for $[Ru@Sn_{12}]^{4-}$ is 0.109 Å. The unit cell of $[K(2.2.2\text{-crypt})]_3[Rh@Sn_{12}]\cdot 2Tol$ contains two $[Rh@Sn_{12}]^{3-}$ cluster units that are isoelectronic with $[Ru@Sn_{12}]^{4-}$, one of which is almost perfectly icosahedral (Rh–Sn = 2.95 Å, Sn–Sn = 3.05–3.09 Å, RMSD = 0.013 Å). The other, shown in Fig. 1, has a much larger RMSD of 0.045 Å and is distinctly elongated along one 3-fold axis, giving six long (2.95 Å) and six rather shorter (2.88 Å) Rh–Sn bonds. The group 10 clusters, $[Ni@Pb_{12}]^{2-}$, $[Pd@Pb_{12}]^{2-}$ and $[Pt@Pb_{12}]^{2-}$, are even closer to perfect icosahedral symmetry, with the M–Pb and Pb–Pb bonds distributed over 0.11 Å and 0.07 Å, respectively and, in the case of the Pd cluster, an RMSD of 0.013 Å. There is, therefore, a clear trend towards greater distortion as the oxidation state of the endohedral metal becomes more negative.

Electronic structure

Our survey of the singlet potential energy surface of $[Ru@Sn_{12}]^{4-}$ was initialised from a perfectly icosahedral geometry and also from a range of similar structures with small distortions imposed along the C_5, C_3 and C_2 axes. In anticipation of a rather flat potential energy surface, we have imposed tight geometry convergence criteria, and have used a very fine integration grid to avoid artefacts due to numerical noise. In all cases, these calculations converged on structures that were very close to the perfect icosahedron, but none had energies lower than the structure where I_h point symmetry was imposed. We conclude, therefore, that the small deviations observed in the converged geometries are an artefact of the

Table 1 Valence electron count (VEC), crystallographic and DFT-optimized bond lengths for members of the $[M@E_{12}]^{z-}$ family (all values in Å)

VEC			*M*–*E* (Å)	*E*–*E* (Å)	N_{imag}	E_{rel} (eV)	Ref.
$[Ru@Sn_{12}]^{4-}$	60	X-ray	2.79–3.03	2.94–3.31			This work
		DFT (I_h)	2.96	3.11	0	0.0	
		DFT (D_{2d})	3.04–3.12	2.85–2.96	0	+1.07	
$[Rh@Sn_{12}]^{3-}$	60	X-ray	2.88–2.95	3.04–3.13			15
		DFT (I_h)	2.96	3.12	0	0	
		DFT (D_{2d})	3.01–3.14	2.83–2.99	0	+1.79	
$[Ir@Sn_{12}]^{3-}$	60	X-ray	2.88–2.94	3.03–3.10			39
		DFT (I_h)	2.97	3.12	0	0	
		DFT (D_{2d})	3.01–3.14	2.83–2.97	0	+1.60	
$[Pd@Pb_{12}]^{2-}$	60	X-ray	2.98–3.09	3.14–3.21			17
		DFT (I_h)	3.09	3.25	0	0.0	
		DFT (D_{2d})	3.12–3.32	2.97–3.14	2	+3.71	
$[Pt@Pb_{12}]^{2-}$	60	X-ray	3.05–3.06	3.20–3.23			40
		DFT (I_h)	3.09	3.25	0	0	
		DFT (D_{2d})	3.12–3.30	2.96–3.13	2	+3.51	
$[Ru@Ge_{12}]^{3-}$	59	X-ray	2.65–2.77	2.44–2.60			41
		DFT (I_h)	2.66	2.80	5	0	
		DFT (D_{2d})	2.71–2.78	2.48–2.62	0	−1.27	
$[Mn@Pb_{12}]^{3-}$	58	X-ray	2.87–3.30	3.10–3.74			24
		DFT (I_h)	3.09	3.25	0	0	
		DFT (D_{3d})	2.90–3.20	3.15–3.42	0	−0.67	
		DFT (D_{2h})	2.90–3.20	3.15–3.42	1	−0.65	
		DFT (D_{2d})	3.22–3.40	2.98–3.10	6	+2.38	
$[Au@Pb_{12}]^{3-}$	62	X-ray	2.84–3.09	3.10–3.25			42
		DFT (I_h)	3.15	3.31	0	0	
		DFT (D_{3d})	3.15–3.17	3.14–3.60	0	−0.66	
		DFT (D_{5d})	3.14–3.17	3.26–3.39	4	−0.12	
		DFT (D_{2d})	2.99–3.46	2.96–3.32	8	+2.08	

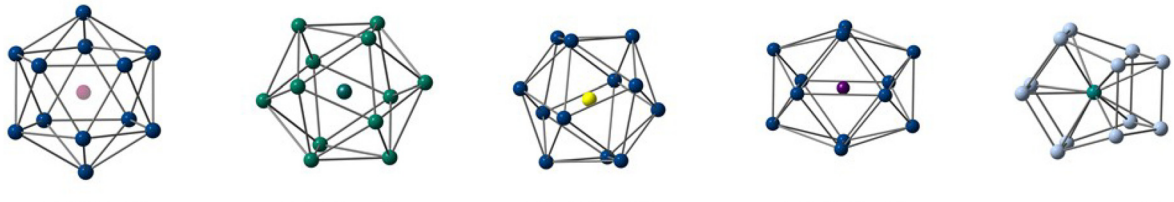

	$[Pd@Pb_{12}]^{2-}$	$[Rh@Sn_{12}]^{3-}$	$[Au@Pb_{12}]^{3-}$	$[Mn@Pb_{12}]^{3-}$	$[Ru@Ge_{12}]^{3-}$
VEC	60	60	62	58	59
	close to perfect I_h	moderately distorted $\sim D_{3d}$	distorted $\sim D_{3d}$	tetragonally elongated $\sim D_{2h}$	fullerene-like $\sim D_{2d}$
M-E/Å	2.98-3.09	2.88-2.95	2.84-3.09	2.87-3.30	2.73-2.80
E-E/Å	3.13-3.21	3.04-3.13	3.11-3.21	3.10-3.74	2.48-2.64
RMSD/Å	0.013	0.045	0.054	0.112	0.602

Fig. 1 Increasing degrees of distortion in approximately icosahedral members of the $[M@E_{12}]^{z-}$ family. The RMSD, a global measure of the degree of distortion of the icosahedron, is defined as the root mean square displacement between the X-ray coordinates and the closest I_h-symmetrized structure. VEC is the valence electron count.

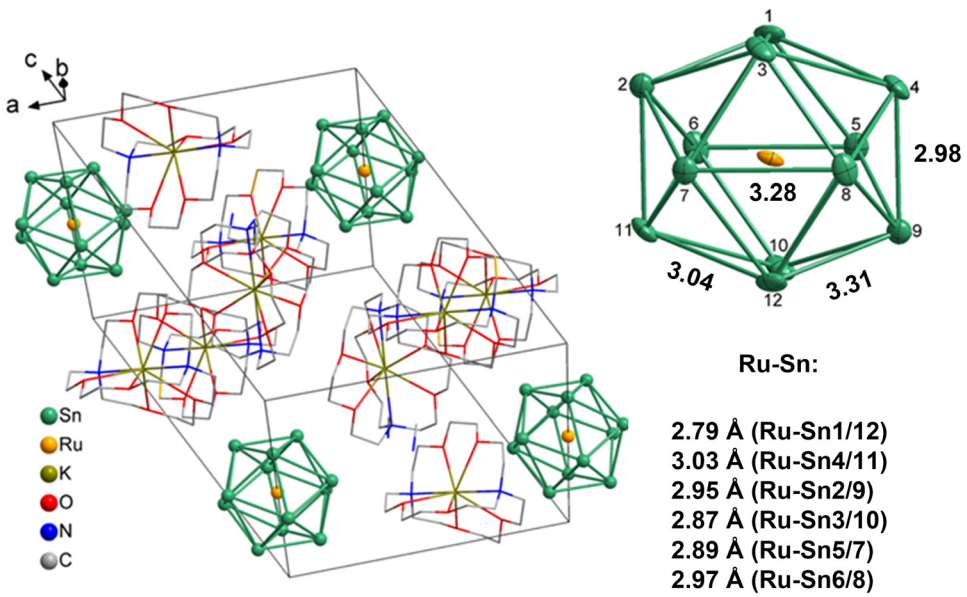

Fig. 2 Unit cell of **1** and the structure of the $[Ru@Sn_{12}]^{4-}$ anion (hydrogen atoms are removed for clarity).

finite convergence criterion, and that the true minimum on the gas-phase potential energy surface is, in fact, the perfect icosahedron. A parallel set of calculations on all the other 60-electron clusters shown in Table 1 followed the same pattern: in no case did we locate a minimum that was more stable than the perfect icosahedron. We conclude, therefore, that the distortions observed in the crystallographic data must be a consequence of the periodic lattice (the averaged effect of which is modelled only very approximately by a high dielectric continuum in our calculations) rather than an intrinsic electronic driving force. Bürgi and Dunitz have established the principle of structural correlation, wherein deformations observed in different crystal structures map on to low-frequency vibrational modes of the equilibrium structure.[43] The computed vibrational spectrum of $[Ru@Sn_{12}]^{4-}$ shows two allowed t_{1u}-symmetric modes at 117 cm^{-1} and 155 cm^{-1} which correspond to the bands at 74 cm^{-1} and 102 cm^{-1} computed for $[Pt@Pb_{12}]^{2-}$ by Cetin *et al.*[44] The 74 cm^{-1} mode has been observed in the experimental FTIR spectrum, while the 102 cm^{-1} mode has been tentatively assigned to a shoulder at

118 cm^{-1}. Of more direct relevance to the low-symmetry distortions in $[Ru@Sn_{12}]^{4-}$ is the mode of h_g symmetry which is real but very small (16 cm^{-1}), increasing to 45 cm^{-1} in $[Rh@Sn_{12}]^{3-}$ and to 68 cm^{-1} in the empty Sn_{12}^{2-} cage. The softening of the mode therefore correlates with the greater magnitude of the distortions to the icosahedron observed in the ruthenium cluster.

The link between the magnitude of the distortion and the enhanced back-bonding in $[Ru@Sn_{12}]^{4-}$ is made explicit in the molecular orbital scheme and associated projected density of states plot shown in Fig. 3. In perfect I_h symmetry the 4d orbitals of Ru transform as h_g, and 4d character is distributed over occupied $1h_g$, $2h_g$ and $3h_g$ as well as the $4h_g$ LUMO+1. The LUMO of the cluster has g_g symmetry, and is therefore not accessible to the electron density in the 4d orbitals. However, the distortion to C_i symmetry found in the X-ray structure allows orbitals of h_g and g_g symmetry to mix, which in turn allows the Ru 4d electrons to filter into the LUMO, rather than LUMO+1, of the cluster. The result is the emergence of a small amount of Ru 4d character in the peak at ~0.7 eV in the right hand panel of Fig. 3. Cui *et al.* have also emphasised the transition of d orbitals from core-like (in Cu/Au) to frontier-like in the earlier metals in their interpretation of the gas-phase photoelectron spectra of a series of endohedral stannaspherenes, $[M@Sn_{12}]^{-}$.[18] Like all the 60-electron clusters reported here, the optimised structures of $[Cu@Sn_{12}]^{-}$ and $[Au@Sn_{12}]^{-}$ are perfectly icosahedral, with the lowest peak in the spectrum corresponding to the $3h_g$ orbital in Fig. 3. The analogues with earlier transition metals are increasingly distorted from the perfect icosahedron, although the measured spectra appear to be rather insensitive to these subtle structural changes.

We have argued previously that very strong back-bonding in $M@E_{12}$ will, ultimately, drive a transition to the fullerene-like D_{2d}-symmetric geometry adopted by $[Ru@Ge_{12}]^{3-}$.[12,26] Given the clear evidence here for enhanced back-bonding in $[Ru@Sn_{12}]^{4-}$ relative to $[Rh@Sn_{12}]^{3-}$ and $[Pd@Pb_{12}]^{2-}$, it is interesting to explore how close to this structural transition the new cluster is. The energies of the D_{2d}-symmetric structures are also included in Table 1, and there is a clear trend towards relative stabilization of this isomer relative to the icosahedron in the order $[Pd@Pb_{12}]^{2-}$ < $[Rh@Sn_{12}]^{3-}$ < $[Ru@Sn_{12}]^{4-}$ (this data is presented in graphical form in the SI, Fig. S5). Nevertheless, the icosahedron remains more stable by over 1.0 eV, even for $[Ru@Sn_{12}]^{4-}$. Extrapolating further back to group 7, we find that the gap between the two isomers narrows to only 0.2 eV for $[Tc@Sn_{12}]^{5-}$ and$[Re@Sn_{12}]^{5-}$. The latter may be a viable synthetic target, and we anticipate unusual dynamic behaviour associated with the close energetic proximity of the icosahedral and fullerene-like isomers.

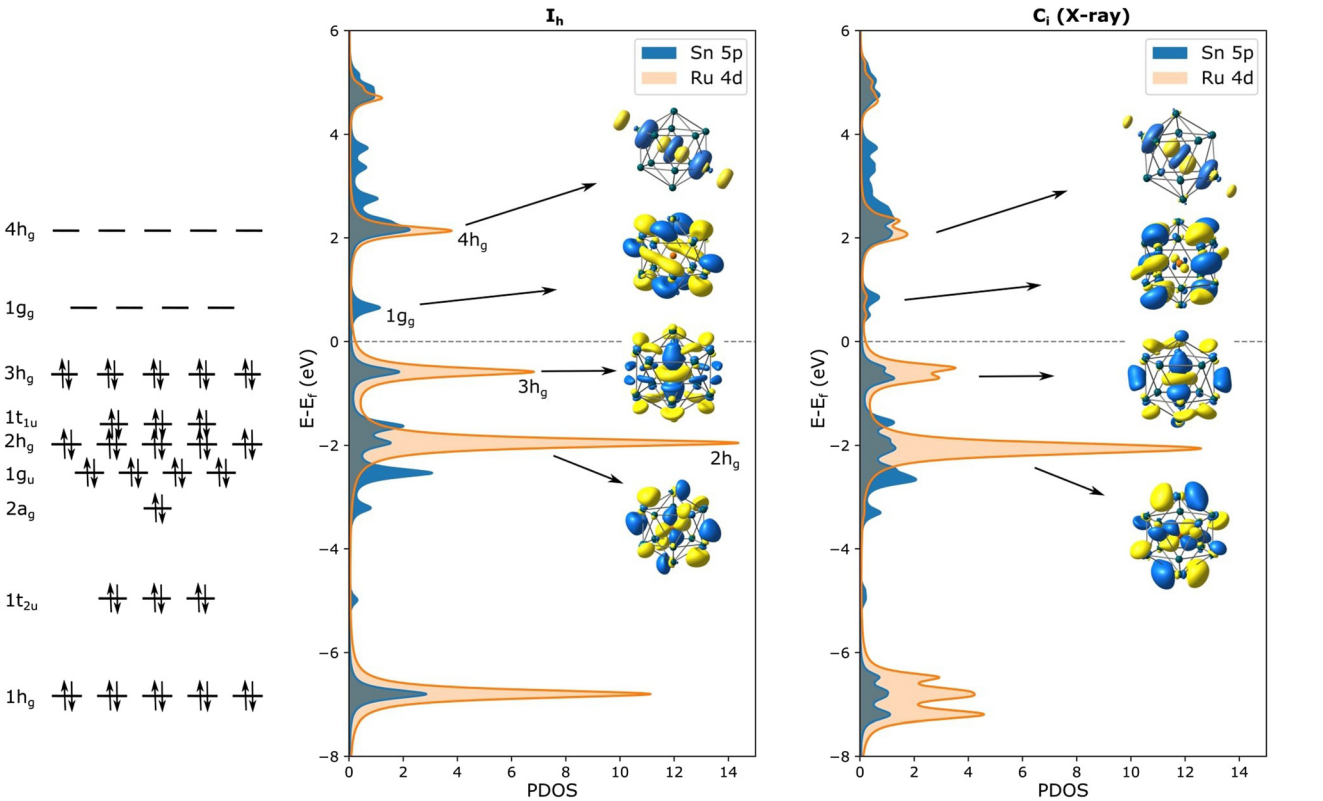

Fig. 3 Kohn–Sham molecular orbitals and projected density of states (PDOS) for $[Ru@Sn_{12}]^{4-}$ in I_h symmetry (left) and at the C_i-symmetric geometry of the X-ray structure (right). The PDOS is per atom of a given type. The Fermi level, E_f, is placed at the mid-point between the HOMO and the LUMO.

Conclusions

In this paper, we have reported the synthesis and structure of a new member of the endohedral icosahedral family, $[Ru@Sn_{12}]^{4-}$. Analogues containing group 9 or group 10 metals (Rh, Ir, Ni, Pd, Pt) are well known, but this work represents the first encapsulation of a group 8 metal into a Sn_{12} cage. The electron-rich group 8 metal is better able to engage in back-bonding to the cage, which softens the lowest frequency h_g-symmetric vibrational mode, making the cluster anion very susceptible to low-symmetry deformations in response to the distribution of cations in the lattice. The cluster anion sits on a centre of symmetry in the $P\bar{1}$ unit cell, and distortions of the icosahedron are pronounced, with the 12 Ru–Sn distances separating out into 6 pairs, ranging from 2.79 Å to 3.03 Å. The group 9 analogues, $[Rh@Sn_{12}]^{3-}$ and $[Ir@Sn_{12}]^{3-}$, are also distorted, but to a lesser extent due to the reduced capacity for back-bonding in the later groups of the transition series.

Author contributions

Y. S.-H.: Investigation, methodology. S. M.: Investigation, methodology, visualization. Z. M. S.: Conceptualization, analysis, funding acquisition, writing – original draft, writing – review & editing. J. E. M.: Conceptualization, analysis, writing – original draft, writing – review & editing.

Conflicts of interest

There are no conflicts to declare.

Data availability

The computational data (energies, optimized coordinates) supporting this article have been included as part of the supplementary information (SI). Supplementary information: full experimental procedures and computational methods, additional crystallographic information, essential spectra and corresponding analyses on $[Ru@Sn_{12}]^{4-}$. The optimized coordinates and supplementary density of states (DOS) plots. See DOI: https://doi.org/10.1039/d5dt02068a.

CCDC 2257232 (**1**) contains the supplementary crystallographic data for this paper.[45]

Acknowledgements

This work was supported by the National Natural Science Foundation of China (22425105, 22371140, 92461303). SM acknowledges the Ministry of Social Justice and Empowerment, Government of India, for a National Overseas Scholarship (K-11015/48/2020-SCD-V/NOS).

References

1 J. Zhao, Q. Du, S. Zhou and V. Kumar, *Chem. Rev.*, 2020, **120**, 9021–9163.
2 B. Weinert and S. Dehnen, *Clusters – Contemporary Insight in Structure and Bonding*, Springer International Publishing, Cham, 2017, pp. 99–134.
3 B. Oelkers, M. V. Butovskii and R. Kempe, *Chem. – Eur. J.*, 2012, **18**, 13566–13579.
4 N. Lichtenberger, R. J. Wilson, A. R. Eulenstein, W. Massa, R. Clérac, F. Weigend and S. Dehnen, *J. Am. Chem. Soc.*, 2016, **138**, 9033–9036.
5 X. Min, I. A. Popov, F.-X. Pan, L.-J. Li, E. Matito, Z.-M. Sun, L.-S. Wang and A. I. Boldyrev, *Angew. Chem., Int. Ed.*, 2016, **55**, 5531–5535.
6 A. R. Eulenstein, Y. J. Franzke, N. Lichtenberger, R. J. Wilson, H. L. Deubner, F. Kraus, R. Clérac, F. Weigend and S. Dehnen, *Nat. Chem.*, 2021, **13**, 149–155.
7 C. Dong, Y. Li, D. Cheng, M. Zhang, J. Liu, Y.-G. Wang, D. Xiao and D. Ma, *ACS Catal.*, 2020, **10**, 11011–11045.
8 X. Jin and J. E. McGrady, *Adv. Inorg. Chem.*, 2019, **73**, 265–304.
9 K. Mayer, J. Weßing, T. F. Fässler and R. A. Fischer, *Angew. Chem., Int. Ed.*, 2018, **57**, 14372–14393.
10 R. J. Wilson, N. Lichtenberger, B. Weinert and S. Dehnen, *Chem. Rev.*, 2019, **119**, 8506–8554.
11 Y. Wang, J. E. McGrady and Z.-M. Sun, *Acc. Chem. Res.*, 2021, **54**, 1506–1516.
12 J. E. McGrady, F. Weigend and S. Dehnen, *Chem. Soc. Rev.*, 2022, **51**, 628–649.
13 B. J. L. Witzel, W. Klein, J. V. Dums, M. Boyko and T. F. Fässler, *Angew. Chem., Int. Ed.*, 2019, **58**, 12908–12913.
14 Y. Wang, C. Zhang, X. Wang, J. Guo, Z.-M. Sun and H. Zhang, *ACS Catal.*, 2020, **10**, 7808–7819.
15 C. Liu, X. Jin, L.-J. Li, J. Xu, J. E. McGrady and Z.-M. Sun, *Chem. Sci.*, 2019, **10**, 4394–4401.
16 J.-Q. Wang, S. Stegmaier, B. Wahl and T. Fässler, *Chem. – Eur. J.*, 2010, **16**, 1793–1798.
17 E. N. Esenturk, J. Fettinger and B. Eichhorn, *J. Am. Chem. Soc.*, 2006, **128**, 9178–9186.
18 L.-F. Cui, X. Huang, L.-M. Wang, J. Li and L.-S. Wang, *Angew. Chem., Int. Ed.*, 2007, **46**, 742–745.
19 L.-F. Cui, X. Huang, L.-M. Wang, D. Y. Zubarev, A. I. Boldyrev, J. Li and L.-S. Wang, *J. Am. Chem. Soc.*, 2006, **128**, 8390–8391.
20 L.-F. Cui, X. Huang, L.-M. Wang, J. Li and L.-S. Wang, *J. Phys. Chem. A*, 2006, **110**, 10169–10172.
21 K. Wade, *J. Chem. Soc. D*, 1971, 792–793.
22 D. M. P. Mingos, *Acc. Chem. Res.*, 1984, **17**, 311–319.
23 L.-J. Li, F.-X. Pan, F.-Y. Li, Z.-F. Chen and Z.-M. Sun, *Inorg. Chem. Front.*, 2017, **4**, 1393–1396.
24 B. Zhou, T. Krämer, A. L. Thompson, J. E. McGrady and J. M. Goicoechea, *Inorg. Chem.*, 2011, **50**, 8028–8037.
25 G. Espinoza-Quintero, J. C. A. Duckworth, W. K. Myers, J. E. McGrady and J. M. Goicoechea, *J. Am. Chem. Soc.*, 2014, **136**, 1210–1213.

26 J. M. Goicoechea and J. E. McGrady, *Dalton Trans.*, 2015, **44**, 6755–6766.
27 X. Jin and J. E. McGrady, *Adv. Inorg. Chem.*, 2019, **73**, 265–304.
28 M. Crocker, M. Green, J. A. K. Howard, N. C. Norman and D. M. Thomas, *J. Chem. Soc., Dalton Trans.*, 1990, 2299–2301.
29 G. M. Sheldrick, *Acta Crystallogr., Sect. A:Found. Adv.*, 2015, **71**, 3–8.
30 O. V. Dolomanov, L. J. Bourhis, R. J. Gildea, J. A. K. Howard and H. Puschmann, *J. Appl. Crystallogr.*, 2009, **42**, 339–341.
31 A. L. Spek, *Acta Crystallogr., Sect. D: Biol. Crystallogr.*, 2009, **65**, 148–155.
32 G. te Velde, F. M. Bickelhaupt, E. J. Baerends, C. Fonseca Guerra, S. J. A. van Gisbergen, J. G. Snijders and T. Ziegler, *J. Comput. Chem.*, 2001, **22**, 931–967.
33 J. P. Perdew, K. Burke and M. Ernzerhof, *Phys. Rev. Lett.*, 1996, **77**, 3865.
34 E. Van Lenthe, A. Ehlers and E.-J. Baerends, *J. Chem. Phys.*, 1999, **110**, 8943–8953.
35 E. Van Lenthe and E. J. Baerends, *J. Comput. Chem.*, 2003, **24**, 1142–1156.
36 C. C. Pye and T. Ziegler, *Theor. Chem. Acc.*, 1999, **101**, 396–408.
37 L. Perring, P. Feschotte, F. Bussy and J. Gachon, *J. Alloys Compd.*, 1996, **245**, 157–163.
38 W.-X. Chen, N. V. Tkachenko, A. Muñoz-Castro, A. I. Boldyrev and Z.-M. Sun, *Nano Res.*, 2022, **15**, 5705–5711.
39 J.-Q. Wang, S. Stegmaier, B. Wahl and T. Fässler, *Chem. Eur. J.*, 2010, **16**, 1793–1798.
40 E. N. Esenturk, J. Fettinger, Y.-F. Lam and B. Eichhorn, *Angew. Chem., Int. Ed.*, 2004, **43**, 2132–2134.
41 G. Espinoza-Quintero, J. C. A. Duckworth, W. K. Myers, J. E. McGrady and J. M. Goicoechea, *J. Am. Chem. Soc.*, 2014, **136**, 1210–1213.
42 L.-J. Li, F.-X. Pan, F.-Y. Li, Z.-F. Chen and Z.-M. Sun, *Inorg. Chem. Front.*, 2017, **4**, 1393–1396.
43 H. B. Bürgi and J. D. Dunitz, in *Structure Correlation; the Chemical Point of View*, John Wiley and Sons, Ltd, 1994, ch. 5, pp. 163–204.
44 A. Cetin, O. Esenturk and E. N. Esenturk, *Eur. J. Inorg. Chem.*, 2017, **2017**, 2413–2421.
45 CCDC 2257232: Experimental Crystal Structure Determination, 2025, DOI: 10.5517/ccdc.csd.cc2frtyz.